Geophysical Research Letters

Supporting Information for

An Optimal Precursor of Northeast Pacific Marine Heatwaves and Central Pacific El Niño events

A. Capotondi[1,2], M. Newman[1,2], T. Xu[2], and E. Di Lorenzo[3]

[1]University of Colorado, Cooperative Institute for Research in Environmental Science.

[2]NOAA Physical Sciences Laboratory.

[3]Georgia Institute of Technology.

Contents of this file

Introduction

We describe in more detail the LIM methodology and the procedure used to compute the optimal precursors of marine heatwaves (MHWs). We then provide additional information on the optimal structures obtained with our LIM over the full domain according to the L2 (Euclidean) norm, and illustrate their patterns and evolution. We also outline the derivation of why the adjoints of the dynamical eigenvectors represent the optimal forcing patterns of the corresponding eigenvectors, and show some results for different optimization times.

Text S1. Calculation of optimal MHW precursors using the LIM

The LIM used in this study describes the system of interest in terms of sea surface temperature and sea surface height anomalies (SSTA, SSHA) over the tropical and North Pacific Ocean (30°S-70°N, 100°E-290°E). The time evolution of the state vector $\boldsymbol{x} = [SSTA\ SSHA]$ is modelled by the stochastically forced linear dynamical system (Penland and Sardeshmukh, 1995; Newman et al., 2011):

$$d\boldsymbol{x}/dt = \boldsymbol{L}\boldsymbol{x} + \boldsymbol{\xi} \quad (1)$$

where $\boldsymbol{L}$ is a dynamical operator encapsulating the linear dynamics of the system, including an implicit linear parameterization of "fast" (decorrelation timescales much shorter that the dominant dynamical timescales) nonlinear processes, and $\boldsymbol{\xi}$ represents a stochastic white noise forcing which may be spatially coherent. For a given initial state $\boldsymbol{x}$(t), the most likely state at a later time $t+\tau$ is given by the homogeneous solution to (1):

$$\boldsymbol{x}(t+\tau) = \boldsymbol{G}(\tau)\boldsymbol{x}(t) = \exp(\boldsymbol{L}\tau)\,\boldsymbol{x}(t), \text{ where } \boldsymbol{G}(\tau) = \exp(\boldsymbol{L}\tau) \quad (2)$$

The propagator $\boldsymbol{G}$ is first computed in terms of the instantaneous and lagged covariance matrices $\mathbf{C}(0)$ and $\mathbf{C}(\tau_o)$, as $\mathbf{G}(\tau_o) = \mathbf{C}(\tau_o)/\mathbf{C}(0)$, where τ_o is a training lag, and then computed for other lags using (2). An important requirement for LIM validation is the independence of the dynamical operator on the chosen τ_o. As is typically done in LIM, the number of degrees of freedom are reduced by projecting the SST and SSH fields onto their leading empirical orthogonal functions (EOFs). We retained 20 SST and 22 SSH EOFs, accounting for 76% of each field's variance, and used a training lag of one month.

The LIM operator $\boldsymbol{L}$ is generally not symmetric -- it is "non-normal" -- and likewise the eigenvectors of $\boldsymbol{L}$ are not orthogonal. Transient anomaly amplification is therefore possible through constructive eigenmode interference, with lag-dependent amplification factor $\gamma(\tau)$:

$$\gamma^2(\tau) = \frac{\boldsymbol{x}(\tau)^T\boldsymbol{N}\boldsymbol{x}(\tau)}{\boldsymbol{x}(0)^T\boldsymbol{D}\boldsymbol{x}(0)} = \frac{\boldsymbol{x}(0)^T\boldsymbol{G}(\tau)^T\boldsymbol{N}\boldsymbol{G}(\tau)\boldsymbol{x}(0)}{\boldsymbol{x}(0)^T\boldsymbol{D}\boldsymbol{x}(0)}, \quad (3)$$

where $\boldsymbol{N}$ and $\boldsymbol{D}$ are norm kernels for the final and initial states, respectively (e.g., Farrell 1988). The initial growing structures are then the right eigenvectors of $\boldsymbol{G}(\tau)^T\boldsymbol{N}\boldsymbol{G}(\tau)$, with $\gamma(\tau)$ the corresponding eigenvalue. In this study $\boldsymbol{D}$ is set to unity. When $\boldsymbol{N}$ is also unity, growth is measured by the Euclidean norm, or "L2" norm, and the growing structures, also known as "optimal structures", encapsulate the dominant dynamical modes that maximize growth of domain-integrated variance of SST and SSH at lag τ. However, $\boldsymbol{N}$ can also be chosen to maximize the amplification of any specific final structure. Here, $\boldsymbol{N}$ will be chosen to define the "MHW-norm", so that (3) is used to determine optimal initial conditions for Northeast Pacific MHW growth. To that end, we first determine an appropriately representative MHW SST anomaly pattern (see section 3.1), and project it into the SST EOF space of the LIM state vector ($\boldsymbol{r}_{SST}$). Then, we insert $\boldsymbol{r}_{SST}$ into a norm vector $\boldsymbol{n}$ in the LIM state space:

$$\boldsymbol{n} = [\boldsymbol{r}_{SST}\ 000\ \ldots.]. \quad (4)$$

$\boldsymbol{n}$ is then normalized to unity and used to create the final norm kernel $\boldsymbol{N}$ used in (3):

$$\boldsymbol{N} = \boldsymbol{n}^T\boldsymbol{n} + \varepsilon\boldsymbol{I}, \quad (5)$$

where $\boldsymbol{I}$ is the identity matrix and ε is a small number (10^{-9}) added to the diagonal for numerical stability.

Text S2. Dominant growing patterns over the tropical and North Pacific

Here we examine the leading optimal structures over the tropical and North Pacific that are captured by our LIM according to the L2-norm. We find two leading growing structures, whose amplification factors $\gamma(\tau)$, also known as "Maximum Amplification" curves (Penland and Sardeshmukh, 1995) show growth ($\gamma > 1$) over periods of several months (Fig. S1a and S2a). The leading structure achieves its maximum amplitude at a lag of 8 months (Fig. S1a), while the second structure reaches a maximum at τ= 5 months (Fig. S2a), with a slow decay afterwards. The associated spatial patterns of SST and SSH, determined for τ=8 months, are shown in Figs. S1b, c for the leading optimal, and Fig. S2b, c for the second optimal, from the initial to the final states.

The first optimal structure describes a "canonical" El Niño event with SST anomalies in the central-eastern equatorial Pacific. At the initial time (Fig. S1b, t=0) the main SST anomalies show well-known SST ENSO precursors, i.e., Pacific Meridional Mode (PMM; Chiang and Vimont, 2004) in the northern subtropics, and the South Pacific Meridional Mode (SPMM; Zhang et al., 2014) in the southeastern tropical Pacific. The evolution of SSH anomalies (Fig. S1c) is also consistent with exchange of heat content between the equatorial and off-equatorial regions as mediated by Rossby wave propagation. Positive SSH anomalies (deeper thermocline) are also present along the US West Coast, and appear to "propagate" northward along the coast with decreasing offshore scale, consistent with the propagation of coastal Kelvin waves.

Time series associated with the SST/SSH patterns in Fig. S1b, c, obtained by projecting the SST and SSH fields at each time step on those patterns, shows a relative high correlation (r=0.72) between the initial and final optimal structures (Fig. S1d). Linear regression of SLP on the SST/SSH time series reveals the associated SLP patterns (black contours in Fig. S1b). At t=0, SLP anomalies exhibit a dipole pattern in the Northern Hemisphere which is similar to the North Pacific Oscillation (NPO; Rogers, 1981; Linkin and Nigam, 2008), but they rapidly evolve to an anomaly pattern corresponding to a deepened and eastward-displaced Aleutian Low, typical of mature El Niño phases.

The second growing structure (Fig. S2) also displays, at the initial time, SST anomalies typical of the PMM, as well as weak positive anomalies along the equator (Fig. S2b). In this case, however, the presence of negative SSH anomalies (shallower thermocline) in the eastern equatorial Pacific (Fig. S2c), favors the development of negative SST anomalies in that area, leading to a final pattern characterized by positive SST and SSH anomalies in the central Pacific and negative anomalies in the eastern Pacific, which is reminiscent of the El Niño Modoki pattern (Ashok et al., 2007). The associated SLP anomalies show a broad dipole pattern in the northern Hemisphere, which appears to persist throughout the duration of the event. The time series associated with this optimal structure (Fig. S2d) emphasize La Niña and central Pacific El Niño conditions. As such, the evolution of the second optimal structure exhibits a negative skewness as found for some indices of Central Pacific ENSO (Capotondi et al., 2020a, and references therein).

Text S3. Eigenmode analysis of the MHW-Optimal

The dynamical operator $\boldsymbol{L}$ is real, but not self-adjoint, namely not equal to its conjugate transpose $\boldsymbol{L}^{\dagger}$. Thus, its eigenvalues are not real, but consist of complex conjugate pairs. The real part of each eigenvalue is always negative, indicative of a decaying behavior. If the imaginary part is different from zero, then the corresponding eigenmode exhibits an oscillatory behavior with decaying amplitude (Newman, 2007; Newman et al., 2009). Fig. S5 shows the spectrum of the eigenvalues of our $\boldsymbol{L}$ operator in frequency-decay time space. Some eigenvalues are real, and located on the y-axis, while the complex conjugate pairs exhibit both negative and positive frequencies.

To identify the predictable dynamics associated with the evolution of our MHW-Optimal, we decompose the state vector associated with the MHW optimal ($\boldsymbol{x}_{\mathrm{MHW}}$) at t=0 in terms of the $\boldsymbol{L}$ eigenvectors:

$$\boldsymbol{x_{MHW}(0)} = \sum_{\boldsymbol{i=1}}^{\boldsymbol{i=N}} \boldsymbol{\alpha_i}\, \boldsymbol{u_i} \qquad (6)$$

where $\boldsymbol{u_i}$ is the i$^{\mathrm{th}}$ eigenvector of $\boldsymbol{L}$, and $\boldsymbol{\alpha_i}$ is the projection of $\boldsymbol{x_{MHW}(0)}$ on the adjoint $\boldsymbol{v_i}$ of $\boldsymbol{u_i}$. The adjoints are the eigenvectors of $\boldsymbol{L}^{\dagger}$, such that $\boldsymbol{u_i} \cdot \boldsymbol{v_j} = \boldsymbol{\delta_{ij}}$ (Newman, 2007). We then selectively remove individual eigenvectors to assess their role in the growth of the optimal. Since we are interested here in events lasting a minimum of 5 months, and in lead times two seasons or longer, we focus on eigenvectors whose decay time is longer than 5 months. These eigenvectors include modes representing different flavors of ENSO (highlighted in color in Fig. S5), whose spatial patterns for the phases of minimum and maximum amplitudes are displayed in Fig. S6. One of the modes has a spatial structure that spans the tropical and North Pacific ("NP-CP" eigenmode), while the two other eigenmodes exhibit anomalies primarily confined in the tropics ("ENSO-4yr" and "ENSO-2yr"). Of these eigenvectors, the "NP-CP" mode provides the largest contribution to the MHW growth, suggesting that $\boldsymbol{x_{MHW}(0)}$ may be very similar to the structures that optimally energize the NP-CP eigenmode. The adjoint of a given eigenmode is its optimal infinite time scale initial condition (Farrell 1988) and is related to its optimal forcing pattern (known as "Stochastic Optimal"; Moore and Kleeman 1999), through its projection on the system noise. Indeed, if we introduce in the LIM equation

$$\boldsymbol{dx/dt = Lx + \xi} \qquad (7)$$

the expansion of the state vector $\boldsymbol{x}$ in terms of the $\boldsymbol{L}$ eigenvectors:

$$\boldsymbol{x} = \sum_{\boldsymbol{i=1}}^{\boldsymbol{i=N}} \boldsymbol{\alpha_i}\,(\boldsymbol{t})\boldsymbol{u_i}, \qquad (8)$$

and multiply the resulting equation by the j$^{\mathrm{th}}$ adjoint vector $\boldsymbol{v_j}$, we can obtain the following equation for the expansion coefficient of the j$^{\mathrm{th}}$ eigenvector:

$$\frac{\boldsymbol{d\alpha_j}}{\boldsymbol{dt}} = \boldsymbol{\lambda_j \alpha_j + \beta_j},$$

where we use the relationship $\boldsymbol{Lu_j = \lambda_j u_j}$, and define $\boldsymbol{\beta_j = v_j \cdot \xi}$, indicating that the

forcing for $\boldsymbol{\alpha_j}$ arises from the projection of the adjoint $\boldsymbol{v_j}$ onto the noise $\boldsymbol{\xi}$.

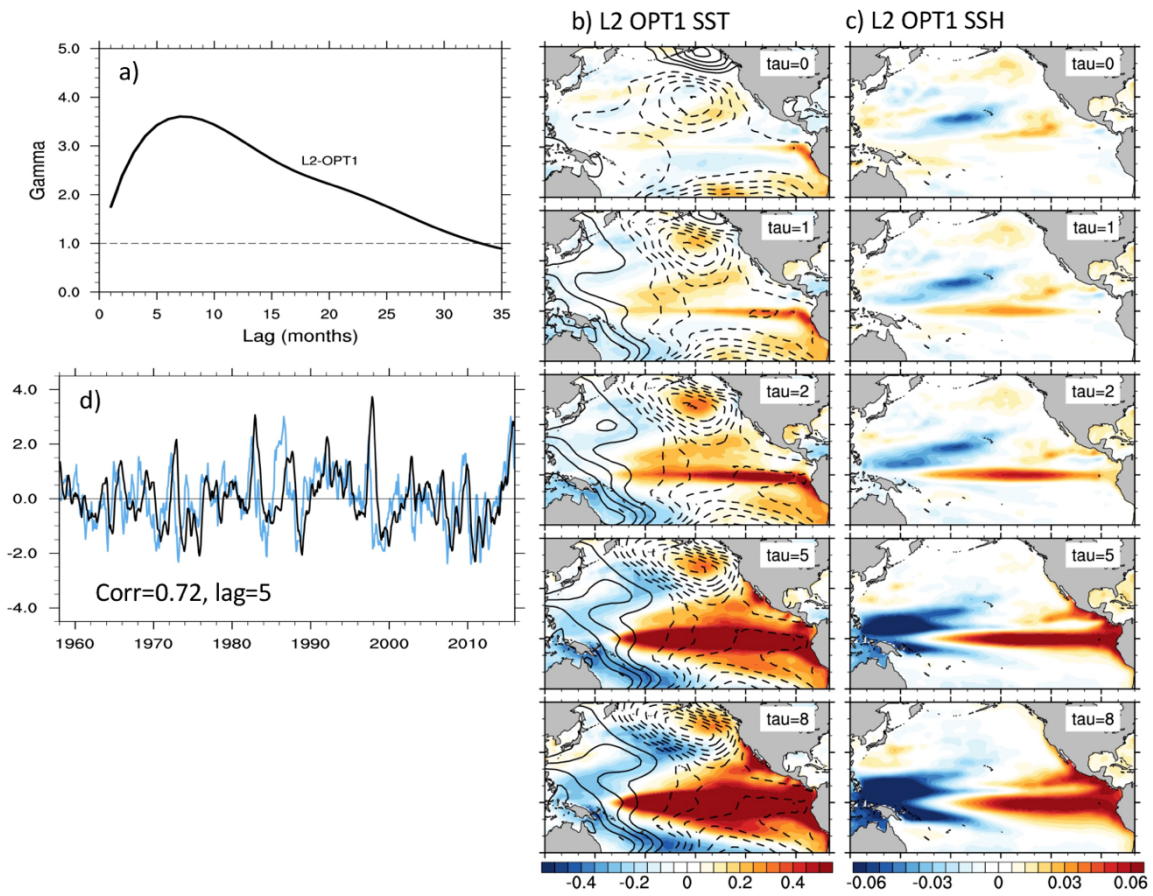

Figure S1. Leading Optimal under the Euclidean (L2) norm. a) "Maximum amplification" curve for the first optimal structure according to the L2 norm. b) Evolution of SST anomalies associated with the leading optimal structure, for an optimization time of eight months, from the initial to final time. Shading is for SST, and black contours for SLP (negative values dashed). c) Evolution of SSH anomalies associated with the leading optimal structure, for an optimization time of eight months, from the initial to final time. d) Time series of the initial (light blue, t=0) and final (black, t=8) leading optimal structures, obtained by projecting the SST/SSH data on the corresponding SST/SSH optimal patterns in b) and c). Correlation coefficients between initial and final conditions are 0.72 when the initial leads the final by 5 months. SST and SSH units are arbitrary. Contour interval for SLP is 0.15.

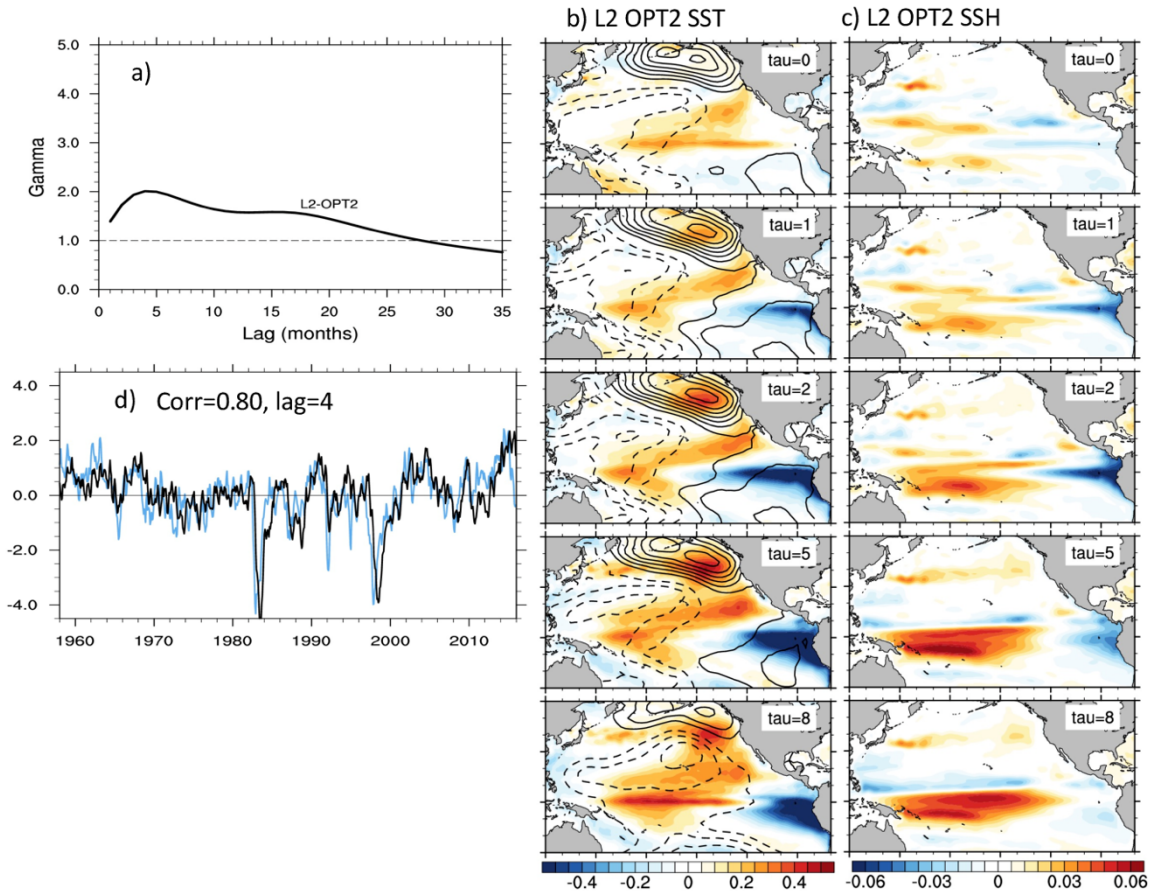

Figure S2. Second leading Optimal under the Euclidean (L2) norm. Same as Figure S1, but for the second LIM optimal. In d), correlation coefficients between initial and final conditions are 0.80 when the initial leads the final by 4 months.

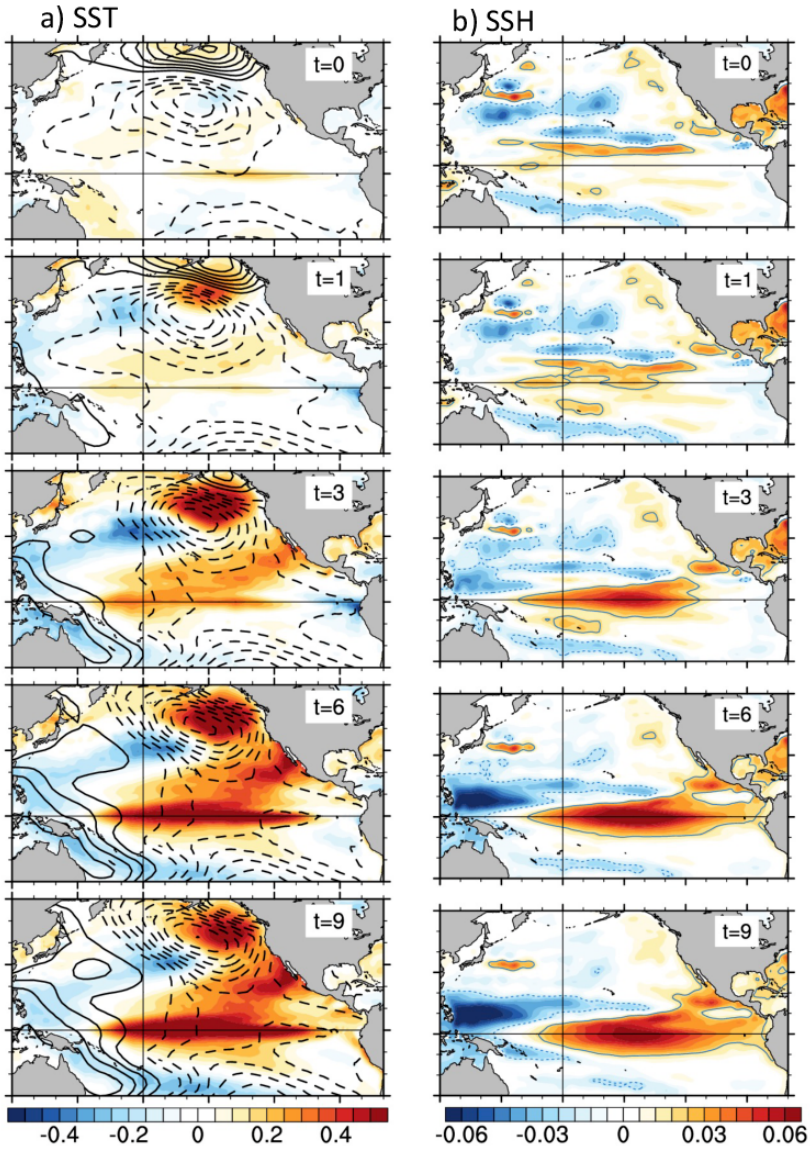

Figure S3. MHW Optimal for optimization time τ = 6 months. a) Evolution of the SST component of the MHW optimal (shading) from t=0 to t=9. Black contours show the regression of SLP on the optimal time series at each time level, with negative values dashed. b) Evolution of the SSH component of the MHW optimal (shading) at tau=6 months. The -0.02 (dashed) and 0.02 (solid) SSH contours are indicated in light blue. SST and SSH units are arbitrary. Contour interval for SLP is 0.15.

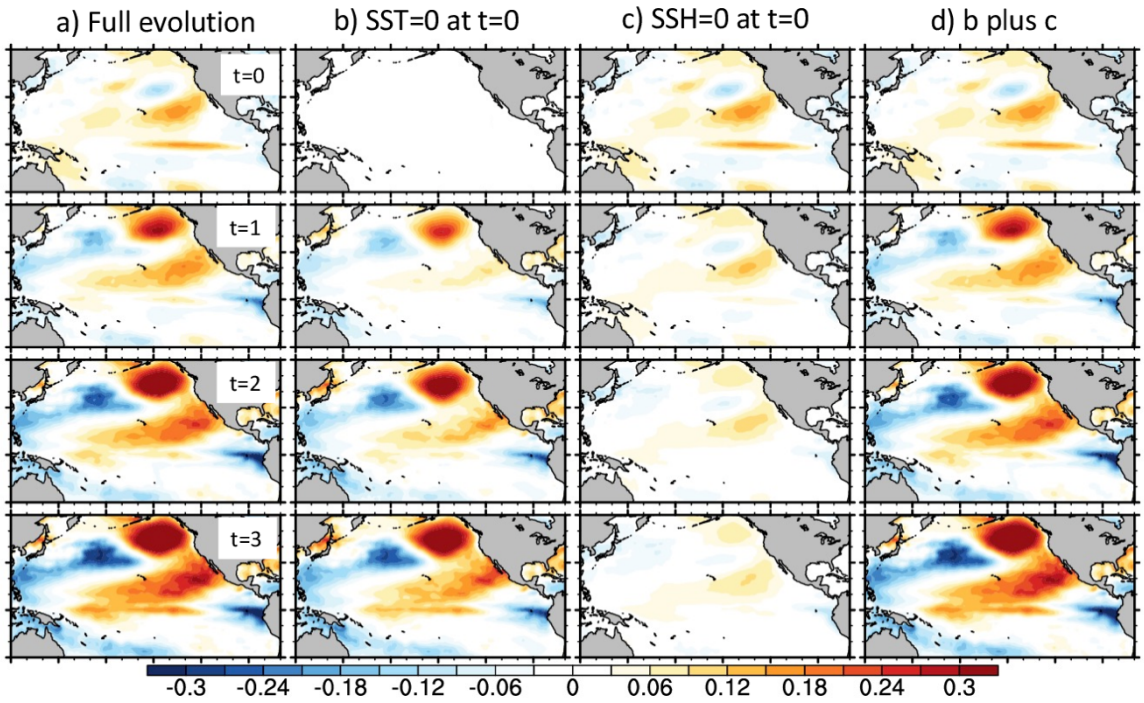

Figure S4. Influence of SST/SSH initial conditions on MHW optimal growth. Evolution of the SST anomalies for the MHW optimal at τ=9 months over the first three months. a) Evolution with initial SST and SSH values equal to the optimal initial values. b) Evolution of SST when initial SST anomalies are set to zero. c) Evolution of SST when the initial SSH values are set to zero. d) Sum of b) and c), reproducing the full evolution in a).

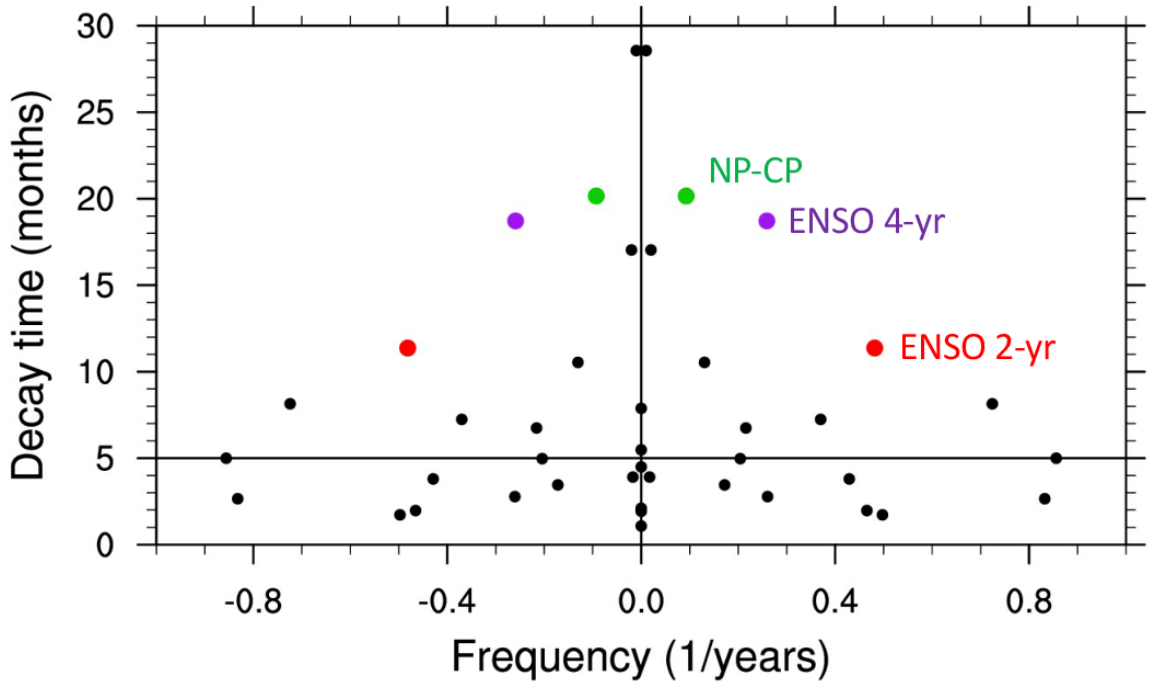

Figure S5. Eigenvalues of ***L***. a) Frequency (x-axis, years^{-1}) and decay time (y-axis, months) of the eigenvalues of the dynamical operator ***L***. Dots on the y-axis with zero frequency are real and correspond to purely decaying eigenmodes, while complex conjugate eigenvalues include both positive and negative frequencies. Three eigenvalues are highlighted: the "NP-CP" eigenmode (Period = 10.8 yrs, decay time= 20 months), the ENSO 4-yr (period: 3.9 years; decay time = 18.7 months), and the "ENSO 2-yr" (period=2 years; decay time=11.4 months). The spatial patterns of the corresponding eigenvectors, which describe different flavors of ENSO, are displayed in Figure S6.

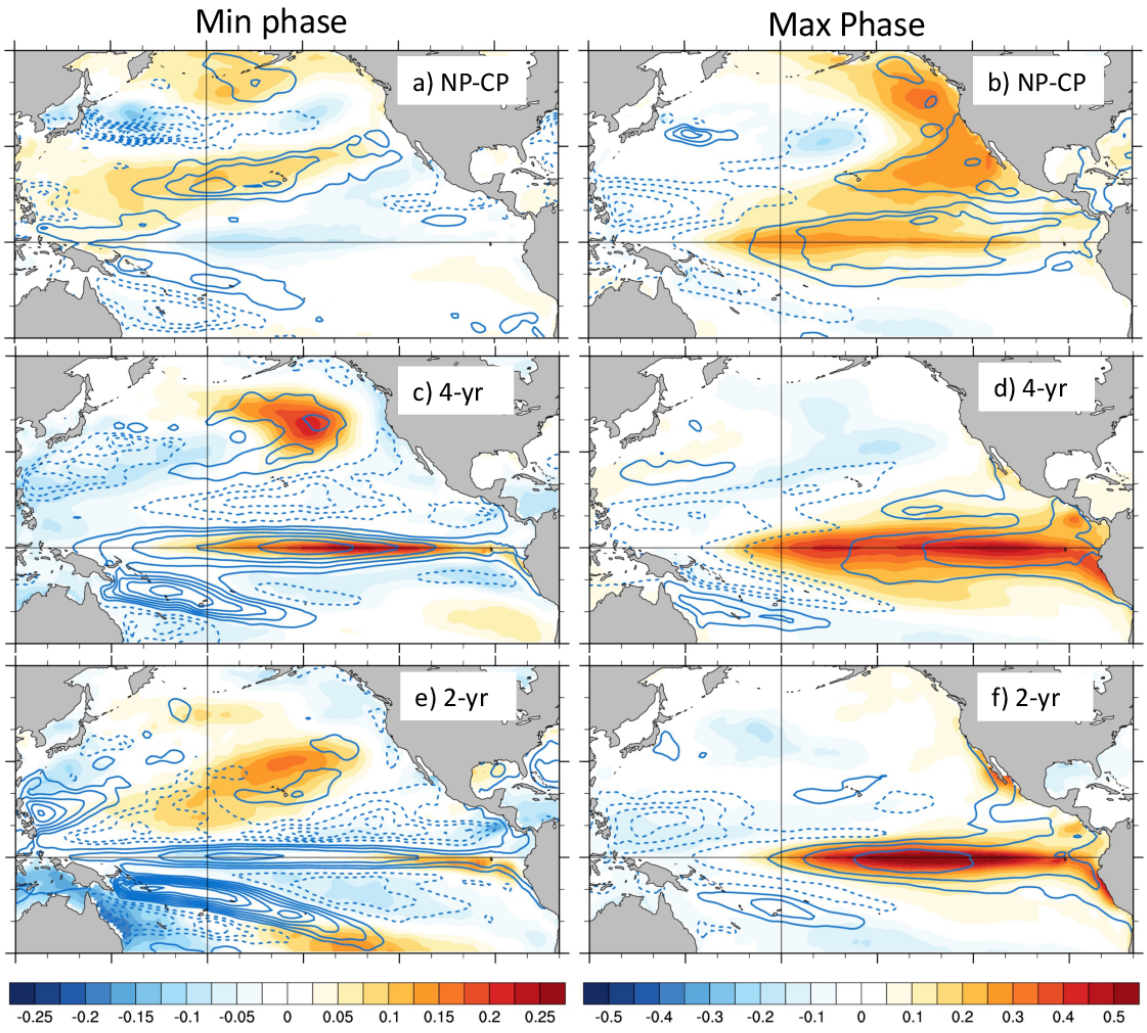

Figure S6. Selected Eigenvectors of ***L***. Complex eigenvectors evolve from a phase of minimum amplitude (left column) to a phase of maximum amplitude (right column). a-b show the two phases of the NP-CP eigenmode, c-d display the ENSO 4-yr eigenmode, and e-f the ENSO 2-yr eigenmode. Shading is for SST, while contours are for SSH. Units are arbitrary, but they are the same for all panels. Contour interval for SSH is 0.005 for the minimum phase and 0.01 for the maximum phase.

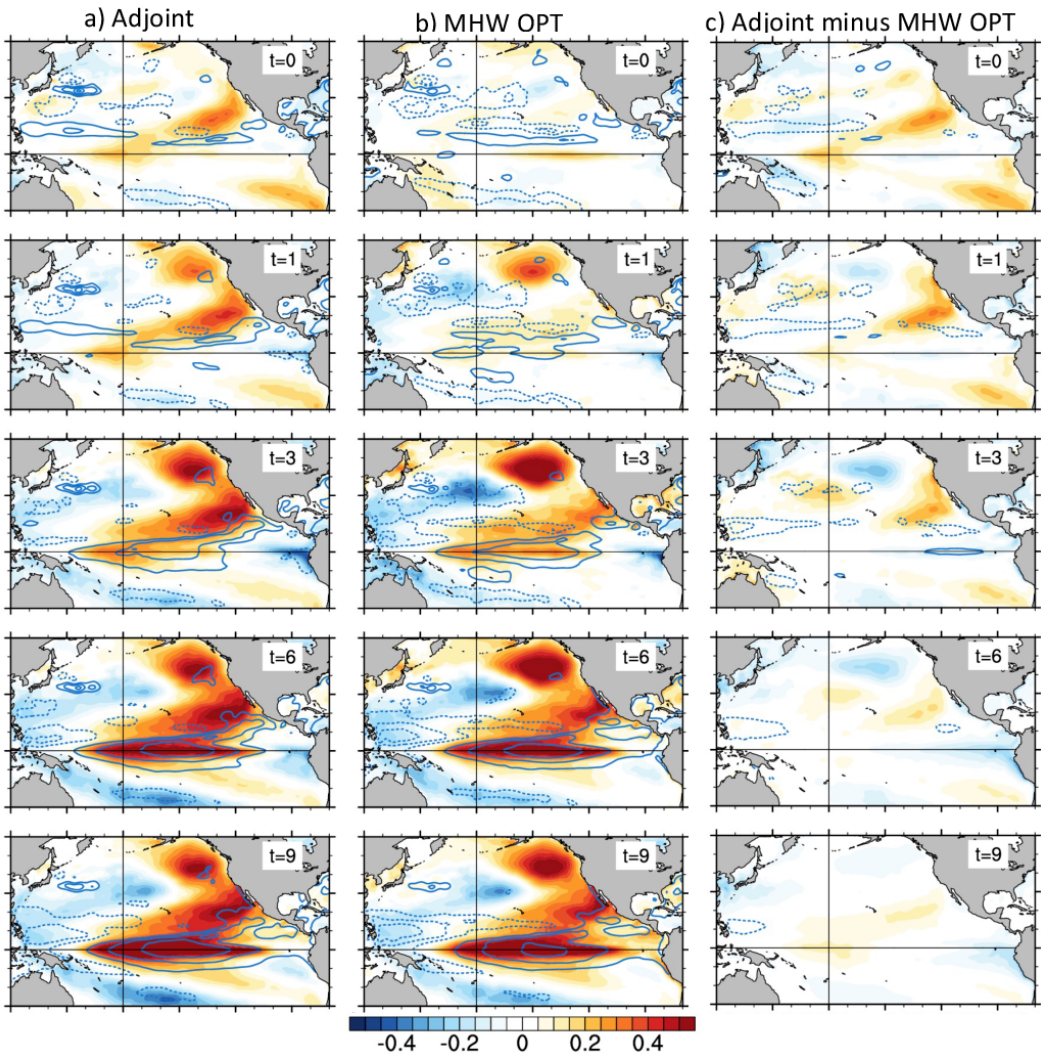

Figure S7. Similar to Fig. 4 but for an optimization time $\tau = 6$ months. a) Evolution starting from the adjoint of the "NP-CP" eigenvector of the dynamical operator. The pattern of the adjoint at time t=0 corresponds to the phase of largest projection on the initial MHW optimal, which is 0.70. Shading indicates SST, while contours are used for SSH. Contour interval is 0.02, with negative values dashed. b) Evolution starting from the MHW optimal for the 6-month optimization time, displayed for comparison with that starting from the adjoint. c) Difference between the evolutions from the adjoint and the MHW optimal. This figure is similar to Figure 4. Notice, however, that the difference between the evolutions from the adjoint and the MHW optimal is larger at shorter times, indicating that other faster decaying eigenmodes may be relatively more important for shorter optimization times.